UNSTABLE CYCLICALLY SYMMETRIC AND STABLE ASYMMETRIC PUMPKIN BALLOON CONFIGURATIONS

Frank Baginski*
George Washington University
Washington, DC 20052
baginski@gwu.edu

Kenneth A. Brakke
Susquehanna University
Selinsgrove, PA 17870
brakke@susqu.edu

Willi W. Schur†
P.O. Box 698
Accomac, VA 23301
pwschur@verizon.net

16 September 2005

Abstract

By design, a pumpkin balloon is intended to assume a cyclically symmetric "pumpkin-like" shape once it reaches float altitude and is fully inflated. Recent work by the authors showed that under certain circumstances, a strained cyclically symmetric pumpkin balloon configuration can be unstable. This means the balloon must assume an alternate non-cyclically symmetric stable equilibrium shape. Julian Nott's round-the-world balloon *Endeavour* was one of the first pumpkin-type balloons to encounter this instability. In this paper, we will explore the phenomena of unstable cyclically symmetric and stable asymmetric balloon configurations. Through numerical computations using our mathematical model for strained balloon shapes, we find asymmetric equilibria that bear a striking resemblance to those observed in ground inflation tests of *Endeavour*. One difficult aspect of modeling such configurations is dealing with the problem of self-contact. By including certain linear constraints in our variational formulation of the problem, we are able to represent balloon configurations with significant regions of self-contact in a way that mimics how a real balloon stores excess material. We apply our finite element model for strained balloon shapes to *Endeavour*-like pumpkin balloons and compute a number of asymmetric equilibrium balloon configurations.

*Senior Member AIAA

†Senior Member AIAA

1 Background

In the late 1980's in the race for the first balloon circumnavigation of the globe, Julian Nott proposed a design that was radically different from his competitors. Nott's design was a constant bulge angle pumpkin balloon called the *Endeavour*. The constant bulge angle pumpkin is described in Section 2. *Endeavour* was a high pressure balloon that was originally designed to have 64 gores. The *Endeavour* did not attain its intended cyclically symmetric equilibrium configuration in its first inflation test on the ground. In fact, when *Endeavour* was pressurized, it assumed the shape seen in Figure 1(a). Nott and his team surmised that the problem was related to excess material. When two gores were removed, the asymmetry was less severe, but still remained (see Figures 1(b)-(c)). Only when four gores were removed did it attain an equilibrium configuration that at least to the eye appeared to be cyclically symmetric. See Figure 1(d). While reducing the number of gores to 60 enabled the balloon to deploy, it is not clear how this balloon would behave over time under normal loading conditions. Nevertheless, the *Endeavour* was later flown at reduced capacity though not in a circumnavigation (see Figure 2).

Even though it was limited to hydrostatic pressure only, Calledine [8] devised a model that attempted to explain the behavior of the fully inflated *Endeavour* in terms of stability. Being limited by computational capabilities of the time, Calledine cleverly observed that in his semi-empirical approach he could ignore the variation in the strain energy contribution to the corresponding variation of the total potential energy. This allowed him to approximate the principle of minimum total potential energy by a maximum volume

rule. Calledine's approximation, even though formulated on the basis of a simple proxy-problem seems to be remarkably accurate. When we compare our stability results on constant bulge angle pumpkin balloons using our full model with the stability results of Calledine [8], we find very good agreement, supporting Calledine's rationale to ignore strain energy contributions in the analysis of *Endeavour*-like balloons. See Section 5. The authors in [10] considered constant bulge radius pumpkin balloons. Similarly to Calledine, they only considered the hydrostatic pressure, ignoring structural weight and strain energy distributions to the total potential energy. While ignoring the strain energy contribution in the analyses of the balloons considered in [8] and [10] was an enabling assumption that provided good first order estimates, this assumption would be grossly in error if the structural materials were undergoing large elastic strains as in balloons made of elastomeric materials. Furthermore, this simplification is also inappropriate when the materials undergo significant visco-elastic deformation over the service life of the balloon, as it will be the case in NASA's Ultra Long Duration Balloon (ULDB) currently under development. NASA's current design scheme for ULDB uses a tri-laminate polyethylene film, which at the maximum internal pressure and temperature the experiences during over-flight periods over hot deserts in the southern hemisphere will accumulate significant creep. Clearly, stability analyses need to be performed on the deformed equilibrium state. In the case of visco-elastic materials this may mean that several equilibrium states need to be examined unless a single equilibrium state can be clearly defined as the most vulnerable to instability.

Analyses are only performed on idealized models. Actual systems are only approximated by such models. Fabrication imperfections and variability in material properties are generally random, so that including them in analytical models is impractical. It is therefore necessary that actual designs fall well inside the stable regime of the feasible design space for a given design class with sufficient margins to the stability threshold. This issue will require analytical study. Obviously, trial and error by designing, fabricating and testing is impractical.

The constant bulge angle assumption in a pumpkin balloon design is a geometrically imposed condition and is not based on global equilibrium principles. It merely facilitates generating a three-dimensional pumpkin-like shape. While some of these designs turn out to be stable, most are unstable. The constant bulge radius pumpkin balloon model presented in [3] is based on an approximation to equilibrium that includes weight and pressure variation. Nevertheless, it can lead as well to and unstable designs under certain circumstances. See Section 5 and the results in [1] for more on the stability of constant bulge radius pumpkin balloons. Moreover, since the balloon film is visco-elastic, a balloon that is stable at the start of its mission could through visco-elastic deformation over time migrate into a configuration that is unstable. See [1] and [2] for further discussions on the stability of pumpkin balloons.

In Section 2, we describe the types of pumpkin balloons that are analyzed in this paper. In Section 3, we outline our finite element model for strained balloons. In Section 4, we define the term stability as used in our work. In Section 5, we present numerical studies on the stability of pumpkin balloon designs. In Section 6, we calculate a few asymmetric stable equilibrium shapes related to the *Endeavour* design. In Section 7, we present concluding remarks.

2 Pumpkin Balloons

In this section, we define pumpkin balloons that are analyzed in this paper. We begin with a description of a constant bulge radius pumpkin that is parametrized as a tubular surface. Next, we consider two pumpkin designs, the Euler-elastica constant bulge radius pumpkin and the Euler-elastica constant bulge angle pumpkin balloon. *Endeavour* was based on the Euler-elastica constant bulge angle design.

Constant bulge radius pumpkin. Let $\boldsymbol{\Upsilon}(s) = R(s)\mathbf{i} + Z(s)\mathbf{k} \in \mathbb{R}^3$ be a planar curve that we call the generator of the pumpkin gore. Apriori $\boldsymbol{\Upsilon}$ is unknown, and must be derived from equilibrium conditions. A detailed exposition of the shape finding equations for a pumpkin balloon, including the determination of $\boldsymbol{\Upsilon}$, is presented in [3].

The generator is parameterized by arc length s, i.e., $|R'(s)|^2 + |Z'(s)|^2 = 1$ where "$'$" denotes differentiation with respect to s. Let $\mathbf{t}$ denote the unit tangent and $\mathbf{b} = \mathbf{t} \times \mathbf{j}$ the inward unit normal of $\boldsymbol{\Upsilon}$; $\theta = \theta(s)$ is the angle between $\mathbf{t}$ and $\mathbf{k}$, and

$$\begin{aligned} \mathbf{t}(s) &= \sin\theta\mathbf{i} + \cos\theta\mathbf{k}, \\ \mathbf{b}(s) &= -\cos\theta\mathbf{i} + \sin\theta\mathbf{k}. \end{aligned}$$

The set $\{\mathbf{b}, \mathbf{t}, \mathbf{j}\}$ gives a right hand curvilinear basis for $\mathbb{R}^3$. The curvature of $\boldsymbol{\Upsilon}$ is κ. We define a tubular surface in the following manner. Let

$$\begin{aligned} \boldsymbol{x}(s,v) &= \boldsymbol{\Upsilon}(s) + r_B\left(\mathbf{j}\sin v - \mathbf{b}(s)\cos v\right), \\ &\quad -\pi < v < \pi, \quad 0 < s < L_d, \end{aligned} \tag{1}$$

$x(s,v) = \boldsymbol{x}(s,v)\cdot\mathbf{i}$, and $y(s,v) = \boldsymbol{x}(s,v)\cdot\mathbf{j}$.

We denote partial differentiation using subscript notation, e.g., $\boldsymbol{x}_s = \partial \boldsymbol{x}/\partial s$. By direct calculation, we have

$$\begin{aligned} \boldsymbol{x}_s(s,v) &= (1 + r_B\kappa(s)\cos v)\mathbf{t}(s), \\ \boldsymbol{x}_v(s,v) &= r_B\left(\mathbf{b}(s)\sin v + \mathbf{j}\cos v\right), \\ \boldsymbol{x}_s \times \boldsymbol{x}_v &= r_B(1 + r_B\kappa(s)\cos v)\left(\mathbf{b}(s)\cos v - \mathbf{j}\sin v\right). \end{aligned}$$

A unit vector normal to the tubular surface is

$$\mathbf{N}(s,v) = \boldsymbol{x}_s \times \boldsymbol{x}_v/|\boldsymbol{x}_s \times \boldsymbol{x}_v| = \mathbf{b}(s)\cos v - \mathbf{j}\sin v,$$

and the triple $\{\boldsymbol{x}_s, \boldsymbol{x}_v, \mathbf{N}\}$ gives a right hand basis for $\mathbb{R}^3$. The principal curvatures of the tubular surface are

$$\begin{aligned} \kappa_1(s,v) &= \frac{\kappa\cos v}{1 + r_B\kappa\cos v}, \\ \kappa_2(s,v) &= \frac{1}{r_B}. \end{aligned} \tag{2}$$

A unit tangent to the curve $s \to \boldsymbol{x}(s,v)$ is

$$\mathbf{a}_1(s,v) = \boldsymbol{x}_s(s,v)/|\boldsymbol{x}_s(x,v)| = \mathbf{t}(s),$$

and a unit tangent to the curve $v \to \boldsymbol{x}(s,v)$ is

$$\mathbf{a}_2(s,v) = \boldsymbol{x}_v(s,v)/|\boldsymbol{x}_v(s,v)| = \mathbf{b}(s)\sin v + \mathbf{j}\cos v,$$

where $\mathbf{t}$ and $\mathbf{b}$ are as previously defined. Note, $\dfrac{\partial \mathbf{a}_2}{\partial v} = \mathbf{b}(s)\cos v - \mathbf{j}\sin v = \mathbf{N}$. Arc length in the tubular surface along a curve parallel to the generator $s \to \boldsymbol{x}(s,v)$ is $\bar{s}$, where $d\bar{s} = (1 + r_B\kappa(s)\cos v)ds$.

A pumpkin gore will be a subset of a tubular surface. We assume that the pumpkin gore is situated symmetrically with respect to the xz plane and interior to the wedge defined by the half-planes $y = \pm\tan(\pi/n_g)x$ with $x \geq 0$. We will refer to r_B as the *bulge radius* of the pumpkin gore. The curve traced by $v \to \boldsymbol{\Upsilon}(s) + r_B(\mathbf{j}\sin v - \mathbf{b}(s)\cos v)$ is a circle lying in the plane with normal $\mathbf{t}(s)$. To find the length of the segment of the circle that forms a circumferential arc in the pumpkin gore, we need to find the values of v where this arc intersects the planes $y = \pm\tan(\pi/n_g)x$. For fixed s and $v > 0$, we find that v must satisfy $y(s,v) = \tan(\pi/n_g)\ x(s,v)$. This leads us to the equation

$$A(s) + B(s)\cos v + C\sin v = 0, \tag{3}$$

where

$$\begin{aligned} A(s) &= -R(s)\tan(\pi/n_g), \\ B(s) &= -r_B\cos\theta(s)\tan(\pi/n_g), \\ C &= r_B. \end{aligned}$$

Solving Eq. (3) for v, we denote the solution by

$$v_B(s) = v_B(s, n_g, r_B, R(s), \theta(s)).$$

In this paper, $v_B(s)$ is called the bulge angle of the constant bulge radius pumpkin balloon. The parameter dependence as well as the dependence on s will be clear from context and so we write $v_B(s)$ for convenience. By symmetry, the solution corresponding to the plane $y = -\tan(\pi/n_g)x$ is $v = -v_B(s)$. We define the theoretical three-dimensional pumpkin gore $\mathcal{G}_F$ to be

$$\mathcal{G}_F = \{(x,y,z) = \boldsymbol{x}(s,v) \mid |v| < v_B(s),\ 0 < s < L_d\}.$$

A complete shape $\mathcal{S}$ has cyclic symmetry and is made up of n_g copies of $\mathcal{G}_F$. Note that the length of the centerline of $\mathcal{G}_F$ is $L_c = \int_0^{L_d}(1 + r_B\kappa(s))ds$ and the length of a tendon is $L_t = \int_0^{L_d}(1 + r_B\kappa(s)\cos(v_B(s))ds$. Corresponding to $\mathcal{G}_F \subset \mathbb{R}^3$ is the lay-flat configuration $G_F \subset \mathbb{R}^2$ shown in Figure 3. The respective centerlines of $\mathcal{G}_F$ and G_F are isometric. The length of a rib in the spine of $\mathcal{G}_F$ is $2r_Bv_B(s)$ and this is the same as the length of a corresponding segment orthogonal to the centerline of G_F. It follows that the corresponding edge of the lay-flat pattern G_F is longer than the tendon length L_t.

Pumpkins based on the Euler-elastica. If we ignore the film weight density and tendon weight density, assume the differential pressure is constant, and assume zero circumferential stress in the natural shape model, we find that $\boldsymbol{\Upsilon}$ can be related to the Euler-elastica curve, i.e.,

$$\theta'' + 2\varrho\sin\theta = 0 \tag{4}$$

where $\varrho = \pi p_0/T_0$, p_0 is the constant differential pressure, and T_0 is the total meridional tension (see [3]). In this case, we find $R(\theta) = \varrho^{-1}\sin\left(\frac{1}{2}\pi - \theta\right)$. This connection was first pointed out by Smalley in his discussion of the e-balloon [14]. $Z(\theta)$ can be found using elliptic functions (see [10]) or by directly integrating $Z'(s) = \cos\theta$. The actual length of the generating curve is determined by Archimedes Principle so that the lift generated by the enclosed gas is equal to the weight of the balloon system.

If we assume that the tendon satisfies an equation of the form (4), then we are led to a constant bulge radius pumpkin balloon that we refer to as the *Euler-elastica constant bulge radius* (EECBR) pumpkin. The EECBR is symmetric about its equator, and is in general, slightly taller and slightly wider than the more general constant bulge radius pumpkin balloon that was defined at the beginning of this section. Once $\mathcal{G}_F$ is determined, a corresponding lay-flat configuration G_F is determined as described in the previous section.

Another pumpkin model involving the Euler-elastica is called the *Euler-elastica constant bulge angle* (EECBA) pumpkin balloon. In the EECBA pumpkin, one assumes, as we did in the EECBR case, that the tendons follow an Euler-elastica curve. However, the region between adjacent tendons is spanned by circular

arcs of constant bulge angle. Eqs. (1)-(2) do not apply to EECBA pumpkin balloons. We will denote the *constant* bulge angle in an EECBA balloon by v_B, and the *varying* bulge angle in an EECBR balloon by $v_B(s)$. From context, it will be clear when v_B is constant and when it depends on s. Thus, if we compare a constant bulge radius pumpkin design with a constant bulge angle pumpkin design, we find the constant bulge angle pumpkin design leads to a gore-width that has significantly more material away from the equator and particularly close to the poles (end-plates). See Figure 4 for a comparison of the EECBA and EECBR lay-flat patterns. The EECBA and EECBR balloons in Figure 4 were designed to lift the same payload. Due to the way in which the respective volumes of the EECBA and EECBR balloons are distributed, the EECBR gore is a bit wider at the equator. In any case, the material distribution in the EECBA pumpkin is problematic, and as a consequence EECBA pumpkin balloons are more prone to be unstable. In the following, we will be discussing only EECBA and EECBR balloons.

3 Finite element model

In this section, we outline the problem of determining the equilibrium shape of a strained balloon. Our model is applicable to any of the pumpkin balloons described in Section 2. We refer the reader to [4] and [5] for a more detailed exposition of our finite element model. We will assume that a balloon is situated so that the center of the nadir fitting is located at the origin of a Cartesian coordinate system. The nadir fitting is fixed, and the apex fitting is free to slide up and down the z-axis. The nadir and apex fittings are assumed to be rigid.

The reference configuration $\Omega \subset \mathbb{R}^2$ for a complete balloon $\mathcal{S} \subset \mathbb{R}^3$ is

$$\Omega = \cup_{i=1}^{n_g} G_i$$

where G_i is isometric to G_F and G_F is determined by the particular design choice (e.g., Euler-elastica constant bulge angle pumpkin or Euler-elastica constant bulge radius pumpkin). In this case,

$$\mathcal{S} = \cup_{i=1}^{n_g} \mathcal{S}_i$$

where $\mathcal{S}_i$ is a deformation of G_i. An equilibrium configuration of a fundamental gore is denoted by $\mathcal{S}_F$. For convenience, we assume that the fundamental gore $\mathcal{S}_F$ is situated symmetrically about the $y = 0$ plane, and contained within the wedge-shaped region $|y| \leq (\tan \pi/n_g)x$, $x \geq 0$, and $z \geq 0$. If $\mathcal{S}$ is a cyclically symmetric balloon shape with n_g-gores, then $\mathcal{S}$ can be generated from n_g copies of $\mathcal{S}_F$, where the corresponding reference configuration is G_F. G_F is assumed to be situated with the bottom of G_F centered at the origin of a (u, v) coordinate system. See Figure 3. Ω and $\mathcal{S}$ are discretized by constant strain plane stress triangular finite elements. Adjacent gores are joined at their common edge. Tendons are located along the edges where adjacent gores are joined.

We will describe our model as it applies to a complete balloon. However, at times we will impose certain symmetry conditions, which will reduce the total number of degrees of freedom in our model. For our stability studies, we typically compute a cyclically symmetric strained equilibrium shape for a fully inflated balloon. Stability of that equilibrium configuration is calculated for the full balloon. For asymmetric shapes, we use the same model but adjust the boundary conditions appropriately.

The total potential energy $\mathcal{E}$ of a strained inflated balloon configuration $\mathcal{S}$ is the sum of six terms,

$$\mathcal{E}(\mathcal{S}) = \mathcal{E}_P + \mathcal{E}_f + \mathcal{E}_t + \mathcal{E}_{top} + S_t^* + S_f^* \qquad (5)$$

where

$$\begin{aligned}
\mathcal{E}_P &= \int_V P(z)dV \\
&= -\int_{\mathcal{S}} (\tfrac{1}{2}bz^2 + P_0 z)\mathbf{k} \cdot \mathbf{n}\, d\sigma \qquad (6)\\
\mathcal{E}_f &= \int_{\mathcal{S}} w_f z dA, \qquad (7)\\
\mathcal{E}_t &= \sum_{i=1}^{n_g} \int_0^{L_t} \boldsymbol{\alpha}_i(S) \cdot \mathbf{k}\ w_t\ dS, \qquad (8)\\
\mathcal{E}_{top} &= w_{top} z_{top}, \qquad (9)\\
S_t^* &= \sum_{i=1}^{n_g} \int_0^{L_t} W_t^*(\epsilon_i) dS, \qquad (10)\\
S_f^* &= \int_\Omega W_f^* dA, \qquad (11)
\end{aligned}$$

$\mathcal{E}_P$ is the hydrostatic pressure potential due to the lifting gas, $\mathcal{E}_f$ is the gravitational potential energy of the film, $\mathcal{E}_t$ is the gravitational potential energy of the load tendons, $\mathcal{E}_{top}$ is the gravitational potential energy of the apex fitting, S_t^* is the total tendon strain energy, and S_f^* is the total film strain energy. For the purpose of the analytical studies in this paper, we assume the differential pressure is in the form $-P(z) = bz + P_0$ where P_0 is known. $V \subset \mathbb{R}^3$ is the region enclosed by $\mathcal{S}$ and dV is volume measure in $\mathbb{R}^3$. We follow the convention that $-P(z) > 0$ means that the internal pressure is greater than the external pressure. P_0 is the differential pressure at the base of the balloon where $z = 0$, b is the specific buoyancy of the lifting gas, $\mathbf{n}$ is the outward unit normal, and $d\sigma$ is surface area measure in the strained balloon surface, w_f is the film weight per unit area, w_t is the tendon weight per unit length, $\boldsymbol{\alpha}_i \in \mathbb{R}^3$ is a parametrization of a deformed tendon with reference configuration Γ_i, w_{top}

is the weight of the apex fitting, z_{top} is the height of w_{top}. The strain in Tendon-i is ϵ_i. $W_t^*(\epsilon_i)$ is the relaxed strain energy density in Tendon-i. W_f^* is the relaxed film strain energy density. Relaxation of the film strain energy density is a way of modeling wrinkling in the balloon film and has been used in the analysis of pumpkin shaped balloons in [4] and [5].

To determine a strained equilibrium balloon shape, we solve the following:

$$\begin{array}{c} \text{Problem } \star \\ \min_{\mathcal{S}\in\mathcal{C}} \mathcal{E}(\mathcal{S}) \end{array} \tag{12}$$

where $\mathcal{C}$ denotes the class of feasible balloon shapes. Boundary conditions or symmetry conditions are built into $\mathcal{C}$. In (12), the continuum problem of finding an equilibrium configuration of the balloon is cast as an optimization problem. This approach is particularly well-suited for the analysis of compliant structures. Problem $\star$ is solved using *Surface Evolver*, an interactive software package for the study of curves and surfaces shaped by energy minimization that was developed by the second author [7]. *Surface Evolver* was used for the analysis presented in [1] and [2]

Remark Self-contact of the balloon film is handled by two mechanisms. First, the vertical planes that bound the sides of the balloon segment are symmetry planes of clefts, and these planes are sticky, in the sense that any surface node that hits one of the planes is thenceforth confined to the plane and cannot pass beyond it. Second, clefts in between the end-planes are handled by checking for each node at the bottom of a groove (originally the tendon nodes) whether the two short horizontal edges emanating from the node have passed each other. If they have, then the two edges are merged to form one edge, and the merged endpoint is now deemed to be at the bottom of a groove. The second mechanism does not permit opposing films to slide on each other, so it may introduce some extra strain, but it doesn't come into play until the perturbations are well-developed, and does not seem to have hindered their development.

4 Stability

The degrees of freedom (DOF) in a faceted balloon shape $\mathcal{S}$ are the x, y, z-coordinates of the nodes of triangular facets $\mathcal{T} \in \mathcal{S}$ that are free to move. Let $\boldsymbol{x} = (x_1, x_2, \ldots, x_N)$ be a list of the DOF. Let $\mathcal{E}(\boldsymbol{x})$ be the total energy of a faceted balloon configuration $\mathcal{S} = \mathcal{S}(\boldsymbol{x})$.

Table 1: Input parameters for pumpkin shape finding.

Description	Value
Tendon weight density (N/m)	0.094
Film weight density (N/m^2)	0.344
Constant differential pressure (Pa)	200

The gradient of $\mathcal{E}$ evaluated at $\boldsymbol{x}$ is the $1 \times N$ vector

$$D\mathcal{E}(\boldsymbol{x}) = \left[\frac{\partial \mathcal{E}}{\partial x_j}\right], j = 1, 2, \ldots, N.$$

The Hessian of $\mathcal{E}$ evaluated at $\boldsymbol{x}$ is the $N \times N$ matrix,

$$H_{\mathcal{E}}(\boldsymbol{x}) = D^2\mathcal{E}(\boldsymbol{x}) = \left[\frac{\partial^2 \mathcal{E}}{\partial x_i \partial x_j}\right], i, j = 1, \ldots, N. \tag{13}$$

Although N can be large for a full balloon, $H_{\mathcal{E}}$ is sparse. The lowest eigenvalue of $H_{\mathcal{E}}$ was calculated by inverse iteration. The matrix $H_{\mathcal{E}} - tI$ was sparse Cholesky factored, with the shift value t chosen to guarantee positive definiteness. The factored matrix was then used to iteratively solve $(H_{\mathcal{E}} - tI)\boldsymbol{x}_{n+1} = \boldsymbol{x}_n$, starting with a random vector $\boldsymbol{x}_0$, until the iteration converged, almost certainly producing the eigenvector of the lowest eigenvalue. See [11, Sec. 11.7, p. 493]. We are led to the following definition of stability.

Definition 4.1 *Let $\mathcal{S} = \mathcal{S}(\boldsymbol{x})$ be a solution of Problem $\star$. We say $\mathcal{S}$ is* stable *if all the eigenvalues of $H_{\mathcal{E}}(\boldsymbol{x})$ are positive. We say $\mathcal{S}$ is* unstable *if at least one eigenvalue of $H_{\mathcal{E}}(\boldsymbol{x})$ is negative. We say that the stability of $\mathcal{S}$ is* indeterminate *if the lowest eigenvalue of $H_{\mathcal{E}}(\boldsymbol{x})$ is zero.*

In principle, the fully inflated shape should be cyclically symmetric so that the loads are distributed uniformly over the entire balloon. If we assume apriori that the strained balloon shape is cyclically symmetric, Problem $\star$ can be solved for a half-gore, and $\mathcal{S}_F$ is determined. $\mathcal{S}_F$ is indeed a stable local equilibrium within the class of cyclically symmetric shapes. However, within the class of complete balloons (call it $\hat{\mathcal{C}}$), the complete balloon generated by $\mathcal{S}_F$ could turn out to be unstable as was demonstrated in [2].

5 Parametric studies

In the following section, we will introduce two sets of parameters denoted by $\mathbf{p}$ and $\mathbf{q}$. Geometry, weight-related, and loading parameters are the elements of $\mathbf{p}$,

while the elements of $\mathbf{q}$ are material properties. The tendon slackness parameter ϵ_t is treated as a material property and is a component of $\mathbf{q}$.

The elements of $\mathbf{p}$ include parameters that are input into the shape finding process for a EECBR pumpkin balloon: n_g, number of gores; r_B bulge radius, etc. In the case of an EECBA pumpkin, the bulge angle v_B is used in place of r_B as a parameter. *Endeavour* was an Euler-elastica constant bulge angle pumpkin balloon. Complete design specifications for *Endeavour* were not available to us, so we selected materials that are commonly used in the fabrication of NASA ultra-long duration balloons. For our demonstrations in this paper, we generated EECBA designs and EECBR designs. For comparisons with the actual *Endeavour* balloon, we found an Euler-elastica with $r_B = 0.979$ m and $n_g = 64$ leads to a bulge angle at the equator of $v_B = 60°$. *Endeavour* utilized a bulge angle of $v_B = 60°$. Nominal parameter values for $\mathbf{p}$ are contained in Table 1. While we assumed $P_0 = 200$ Pa in our studies, *Endeavour* with its stronger balloon fabric and Kevlar tapes was capable of containing differential pressures on the order of 20 mb.

Typically, material properties such as film modulus and Poisson ratio do not enter directly into the shape finding process. Once a set of values are assigned to $\mathbf{p}$, the corresponding pumpkin gore shape $\mathcal{G}_F(\mathbf{p})$ is found, and the lay-flat pattern $G_F(\mathbf{p})$ is determined along with other quantities such as the total system weight, volume, tendon length and seam length of the lay-flat gore pattern, as outlined in Section 2. The three-dimensional shape $\mathcal{G}_F(\mathbf{p})$ is discretized into a collection of triangular facets (call it $\mathcal{G}_F(\boldsymbol{x};\mathbf{p})$), and $\mathcal{G}_F(\boldsymbol{x};\mathbf{p})$ is used as the initial guess for solving Problem $\star$ and determining the corresponding strained equilibrium shape of the fundamental gore $\mathcal{S}_F$. Once $\mathcal{S}_F$ is determined, we then use the cyclic symmetry of the balloon to generate a complete shape $\mathcal{S}$ from n_g copies of $\mathcal{S}_F$. A cyclically symmetric complete balloon generated from $\mathcal{G}_F$ will be denoted by $\mathcal{S}_d(\mathbf{p})$.

We are most interested in investigating the stability of equilibrium configurations of pumpkin designs as a function of (n_g, r_B) for EECBR pumpkins and (n_g, v_B) for EECBA balloons. For this reason, we define the following family of balloon designs,

$$\Pi_d = \{(\mathcal{S}_d(\mathbf{p}), \Omega(\mathbf{p})) \mid \bar{r}_B(n_g) < r_B < \infty\} \qquad (14)$$

where $20 \le n_g \le 200$, $\bar{r}_B(n)$ is the smallest possible bulge radius for a design with n gores in class Π_d. For EECBR pumpkin balloons, $\bar{r}_B(n) = \max(R)\sin(\pi/n)$. For convenience, we will refer to a particular design in Π_d, by indicating the number of gores and the bulge radius. For example, $\Omega(n_g, r_B)$ with $n_g = 64$ and $r_B = 0.979$ m refers to an EECBR pumpkin that is similar in size to *Endeavour*.

Table 2: Material properties for case studies.

Description	Value
Film Youngs modulus (MPa)	202
Film Poisson ratio	0.830
Tendon stiffness (kN)	650

Π'_d denotes the class of EECBA balloon designs

$$\Pi'_d = \{(\mathcal{S}_d(\mathbf{p}), \Omega(\mathbf{p})) \mid 30° \le v_B \le 90°\}$$

where $20 \le n_g \le 100$. There was no need to go beyond 100 gores for the EECBA balloons since they were all unstable for $n_g \ge 100$. A lay-flat pattern in the family Π'_d will be denoted by $\Omega(n_g, v_B)$. It will be clear from context what type of balloon design is being discussed. $\Omega(n_g, v_B)$ with $(n_g, v_B) = (64, 60°)$ corresponds closest to the *Endeavour*.

Once a design has been defined, then we can carry out a stress analysis of that design for some loading condition. For this analysis, we include the full set of material properties, i.e., E_f, film Youngs modulus; ν, film Poisson ratio; K_t, tendon stiffness; and ϵ_t, tendon slackness, etc.. The vector $\mathbf{q}$ includes parameters that were not used directly in the shape finding process. Nominal values for $\mathbf{q}$ are presented in Table 2. Once $\mathbf{p}$ and $\mathbf{q}$ are specified, we can proceed to solving Problem $\star$. Note, the shape determination process and the stress analysis process are separate, and so it is possible to use one value of a parameter in the shape finding process, and another value in the solution of Problem $\star$. The shape finding process defines the lay-flat pattern $\Omega(\mathbf{p})$ and provides a three dimensional shape $\mathcal{S}_d(\mathbf{p})$ that is used for initializing the solution process for Problem $\star$. The strained equilibrium shape that is a solution of Problem $\star$ is denoted $\mathcal{S}(\mathbf{p}, \mathbf{q}, \Omega(\mathbf{p}))$. After solving Problem $\star$ with a design $(\mathcal{S}_d, \Omega) \in \Pi_d$ or $(\mathcal{S}_d, \Omega) \in \Pi'_d$, we will then classify the resulting strained equilibrium configuration according to Definition 4.1.

Remarks

1. We carried out analyses using a complete balloon, and compared these to analyzes carried out using one-half a balloon, i.e., assuming a balloon has one plane of reflectional symmetry. We found that there were roughly twice as many unstable modes for the complete balloon than there were for one-half a balloon. However, after classify-

ing the corresponding designs as stable or unstable, we found both approaches led to roughly the same stability results. This is to be expected due to symmetry breaking of two-dimensional eigenspaces of the full balloon. Thus, we would arrive at roughly the same unstable region if either a full or half balloon were analyzed. To reduce computation time, we analyzed one-half a balloon in our stability studies.

2. We note that stability of an equilibrium configuration is investigated at a strained equilibrium state. In general, a strained equilibrium shape is only approximately a cyclically symmetric constant bulge radius surface. Other strained equilibrium states (due to pressure variations or visco-elastic straining over time) depart from the cyclically symmetric constant bulge radius configuration even more. In the case of a visco-elastic film, that departure can be significant. As shown in [2] by way of looking at different classes of balloon designs, this shape change can have profound effect on stability.

Previous analytical work by the authors showed that for n_g sufficiently small, a minimum bulge radius design that approaches the lower bound is robustly stable. This has been demonstrated in the exploratory work of [13] for 48 gore test vehicles and is demonstrated analytically in [2] for even larger n_g. Calledine (see [8]) showed that for constant bulge shape designs, increasing the number of gores increases vulnerability to instability of the cyclically symmetric configuration.

We analyzed EECBA balloon designs in Π_d' for nominal parameter values. The results are shown in Figure 5(a). In Figure 5, if a design $\Omega(n_g, v_B)$ is unstable, then the point with coordinates (n_g, v_B) is covered with a disk. A design that is stable is covered with a circle. We see from Figure 5(a) that an EECBA pumpkin balloon with *Endeavour*-like parameters clearly lies in the unstable region. For comparison purposes, we considered designs in which the gore pattern is widened by 2 cm. The stable and unstable designs are indicated in Figure 5(b). We find that the number of unstable designs increases when the gore width is increased. We compared our stability results obtained using our full model (Eqn. (5)) with Calledine's model that only includes hydrostatic pressure. In Figure 5, we plot two stability curves that are derived by Calledine, $v_B = (34/n)^{2/5}$ (a curve appropriate for a 64 gore design, see [8, Eq. (26)]) and

$$v_B = (47/n)^{2/5} \tag{15}$$

(a curve that is appropriate for a 60 gore design, see [8, Eq. (27)]). From Figure 6(a), we see that our results on EECBA balloons are in very close agreement with Calledine, supporting his assertion that for constant bulge angle designs and small strains it is appropriate to ignore the film strain energy and load tendon strain energy in a stability analysis of the fully inflated EECBA balloon. Calledine's model does not do so well for the constant bulge radius pumpkins (see the next paragraph). Furthermore, large strains whether elastic or visco-elastic limit the usefulness of Calledine's approach.

We generated Π_d, a class of constant bulge radius pumpkin balloons of comparable size to those in Π_d', and determined the stability of these designs. We found that all designs in Π_d were stable. See Figure 6(a). When we increased the gore width by 1 cm, we found that for $142 \leq n_g \leq 200$ and $r_B < 0.4$ m, some equilibrium configurations were found to be unstable. See Figure 6(c). Note, that even with a 1 cm perturbation, the constant bulge radius pumpkin balloons are stable for $n_g < 142$. A constant bulge radius pumpkin balloon similar in size to the *Endeavour* falls well inside the stable region. In Figure 6(a) and (c), we present our results in terms of (n_g, r_B). For each design in Π_d, we calculated the maximum chord ratio,

$$\Delta = \max_{0 \leq s \leq L_d} \frac{2 r_B v_B(s)}{2 r_B \sin v_B(s)}, \tag{16}$$

where we see that $1 \leq \Delta \leq \frac{1}{2}\pi$. The maximum value of Δ is taken at the equator, and $v_B(s)$ decreases as one nears the end plates. Stability results are presented in terms of (n_g, Δ) in Figures 6(b) and (d). In [15], the authors observed relation (16), substituted $v_B(n) = (47/n)^{2/5}$ into it, and then asserted designs that fell above the curve $(n, (47/n)^{2/5} / \sin(47/n)^{2/5})$ were unstable, and those that fell below this curve were stable (see [15, Fig. 6]). This curve is reproduced in Figures 6(b) and 6(d) which clearly indicates that $(n, (47/n)^{2/5} / \sin(47/n)^{2/5})$ is not a reliable indicator of instability for EECBR balloons. See [1] and [2] for more on comparisons of analytical predictions with flight and experimental data.

6 Asymmetric equilibria

If a cyclically symmetric shape is unstable, an alternate equilibrium configuration must exist. We used *Surface Evolver* to explore the set of alternative equilibria. We are motivated by the photographs of *Endeavour* and the work of [13] to seek shapes with a certain wave number k. The wave number is the number of waves in a complete balloon and in this case, we say the shape has k-fold symmetry. For example, in Figure 1(a)-(c), it appears that *Endeavour* assumed a shape with $k = 1$. For our case studies, we assumed a design with $n_g = 64, v_B = 75°$, and $r_B = 0.848$ m at

Table 3: Total energy of Endeavour-like balloons with p gores per half-section; S - cyclically symmetric; $r = 64 \pmod{2p}$ is the number of gores per gap.

p	r	E [kJ]	V [m^3]	Symmetry
1/2	0	-6,261	15,631	S
4	0	-6,261	15,631	8-fold/S
5	4	-6,263	15,650	-
6	4	-6,270	15,680	-
7	8	-6,279	15,705	-
8	0	-6,285	15,719	4-fold
9	10	-6,288	15,726	-
10	4	-6,287	15,721	-
11	2	-6,284	15,713	-

the equator. To begin our studies, we computed equilibrium configurations for collections of p gores with $p = \frac{1}{2}, 4, 5, \ldots, 11$ (see Table 3). If $2p$ does not divide 64, there is a gap of $r = 64 \pmod{2p}$ gores, since the collection of p gores does not generate a closed shape. Note, when $p = \frac{1}{2}, 4$, or 8, we find the collection of p gores generates a complete balloon. An evolved equilibrium fundamental section with $p = 4$ is presented in Figure 7. The complete balloon is presented in Figure 8. Our approach to handling self-contact works very well. As Figure 7 shows, our asymmetric shapes have no "internal tubes" or regions of self-intersection inside the balloon.

For high values of p, the gore structure becomes invisible and it is possible to compute shapes with wave numbers that are not necessarily divisors of 64. Since it is possible for some tendons that lie in a symmetry plane (where excess film is stored) to become slack or nearly slack, shapes with a variety of wave numbers are not unexpected. For example, to compute a shape with $k = 3$, we use the $p = 10$ solution in Table 3 to generate an initial configuration. In order to insure that the resulting shape has no gaps, we must work with a minimum of 32 gores. An equilibrium configuration with three-fold symmetry is shown in Figure 9. In this case, we find $E = -6,285$ kJ and $V = 15,713$ m^3.

Even though the shapes with four-fold and three-fold symmetry have lower energy than the cyclically symmetric shape in Table 3, we do not claim that the balloon will assume either of these configurations or even the one of lowest energy. Shapes with three-fold and four-fold symmetry are but two of the possible alternative states that are stable local minima. What we can say is that when the cyclically symmetric shape is unstable, it would be impossible for it to be observed.

Remarks

1. For high values of p, we found that the shapes all developed higher wave number instabilities eventually on top of the half-wave mode that was being studied. Typically, the magnitude of the half-wave mode got relatively large before the higher wave mode appeared, and didn't evolve back to the pure higher-wave-number mode. This could have been an artifact of the anti-penetration scheme that was implemented.
2. It is interesting to note that when $p = 4$, the evolved collection of 4 gores generates a balloon shape with eight-fold symmetry that is identical to the cyclically symmetric shape found in the case $p = \frac{1}{2}$.
3. Even though *Endeavour* was inflated at a pressure much higher than $P_0 = 200$ and used different materials, there is a striking similarity between the images in Figures 8-9 and Figures 1(b)-(c).

7 Conclusions

If a fully inflated cyclically symmetric balloon configuration is unstable, then it must assume an alternate stable asymmetric configuration. We explored this phenomena using an Euler-elastica constant bulge angle pumpkin balloon similar in size to Julian Nott's *Endeavour* balloon. By introducing linear constraints to handle the problem of self-contact, we were able to solve a formulation of the balloon problem and calculate asymmetric equilibria, including those with four-fold and three-fold symmetry. Our computed shapes bear a striking resemblance to the asymmetric shapes that have been observed in ground inflation tests of small balloons intentionally fabricated with excess material (see [13]) and some of the *Endeavour* configurations (see Figure 1). In addition, we carried out a stability analysis of a class of Euler-elastica constant bulge angle pumpkin balloons and a comparable class of Euler-elastica constant bulge radius pumpkin balloons. We found that an *Endeavour*-like (EECBA) design was much more likely to have an unstable fully inflated cyclically symmetric equilibrium than an Euler-elastica constant bulge radius pumpkin balloon of com-

parable size. Our stability results on the EECBA pumpkin balloons studies are in close agreement with Calledine's 1988 stability work. While reducing the number of gores from 64 to 60 was a quick fix for the obvious *Endeavour* deployment difficulties, similar, but much more subtle difficulties, are yet to be resolved for the deployment of large NASA ultra-long-duration pumpkin balloons. While it is clear, that it would be impossible for a large pumpkin balloon that is based on an unstable design to achieve a cyclically symmetric configuration at float, it has yet to be demonstrated that a stable design will deploy with any consistency. Moreover, even if such a balloon were to deploy, other hurdles due to the mid-latitude long-duration aspects of flight will need to be overcome. Uncertainties that arise with our predictions come from the fact that the film for the gas envelope for NASA's ULDB is nonlinearly visco-elastic and that cost-effective fabrication introduces significant structural imperfections. The former is difficult to include accurately in the analysis. The latter is impossible to accurately account for in a deterministic way. Both of these aspects, however, can be treated satisfactorily using the tools and techniques utilized in this paper. What is needed is a series of analyses that bound the problem. Both aspects, visco-elasticity and the effect of structural imperfections, require exploratory sensitivity analysis prior to settling on a design class for which safe design guidance can be provided.

Acknowledgments The authors would like the thank Julian Nott for providing photographs of *Endeavour*.

References

[1] F. Baginski, K. Brakke, and W. Schur, *Cleft formation in large pumpkin balloons*, to appear in Advances in Space Research.

[2] F. Baginski, K. Brakke, and W. Schur, *Stability, Clefting and Other Issues Related to Undesired Equilibria in Large Pumpkin Balloons*, AIAA-2005-1803, 6th AIAA Gossamer Spacecraft Forum, April 2005.

[3] F. Baginski, "On the design and analysis of inflated membranes: natural and pumpkin shaped balloons," SIAM Journal on Applied Mathematics, **65** No. 3 (2005), 838-857.

[4] F. Baginski and W. Schur, "Undesired equilibria of self-deploying pneumatic envelopes," to appear in the AIAA Journal of Aircraft.

[5] F. Baginski and W. Schur, "Structural Analysis of Pneumatic Envelopes: A Variational Formulation and Optimization-Based Solution Process," *AIAA J.*, Vol. 41, No. 2, February 2003, 304-311.

[6] F. Baginski and W. Collier, "Modeling the shapes of constrained partially inflated high altitude balloons," *AIAA J.*, Vol. 39, No. 9, September 2001, pp. 1662-1672. Errata: *AIAA J.*, Vol. 40, No. 9, September 2002, pp. 1253.

[7] K. Brakke, *The Surface Evolver*, Experimental Mathematics **1**:2 (1992) 141-165.

[8] C. R. Calledine, "Stability of the Endeavour Balloon" in Buckling of Structures, I. Elishakoff et al., eds., Elsevier Science Publishers, (1988) 133-149.

[9] W. G. Collier, " Estimating stresses in a partially inflated high altitude balloon using a relaxed energy," Quarterly of Applied Mathematics, Vol. 61 No. 1 (2003) 17-40.

[10] A. Lennon and Pellegrino, S. (2000) "Stability of Lobed Inflatable Structures," AIAA-2000-1728, 41st AIAA/ASME/ASCE/AHS/ASC Structural Dynamics, and Materials Conference and Exhibit, Atlanta, GA, April 2000.

[11] W. Press et al, Numerical Recipes in C, 2nd ed., Cambridge University Press, 1992.

[12] A. C. Pipkin, "Relaxed energy densities for large deformations of membranes," IMA Journal of Applied Mathematics, Vol. 52, 1994, pp. 297-308.

[13] W. W. Schur , and C. H. Jenkins, "Deployment destiny, stable equilibria, and the implications for gossamer design", AIAA-2002-1205, 43nd AIAA/ASME/ ASCE/AHS/ASC Structures, Structural Dynamics and Materials Conference and Exhibit, Denver, CO, April 2002.

[14] Justin H. Smalley, "Development of the e-Balloon", National Center for Atmospheric Research, AFCRL-70-0543, Boulder Colorado, June 1970.

[15] M. S. Smith and E. L. Rainwater, Optimum designs for super-pressure balloons, Adv. Space Res., **33** (2004) 1688-1693.

Figure 1: Inflation tests involving *Endeavour*.

(a) 64 Gores

(b) Two gores removed

(c) Two gores removed

(d) Four gores removed

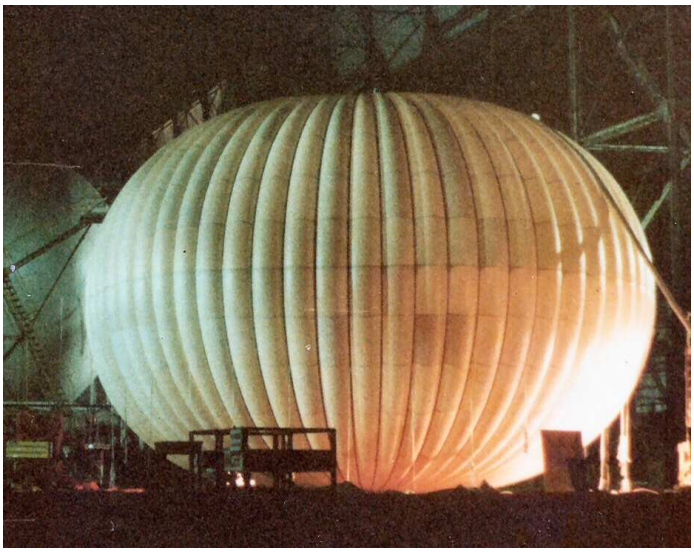

Figure 2: *Endeavour* flight at reduced capacity.

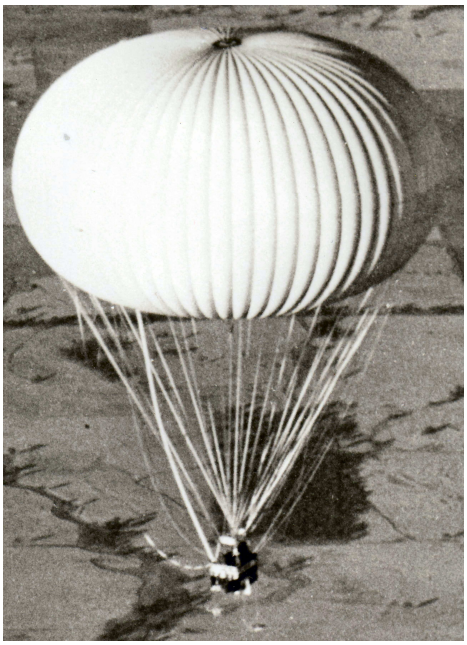

Figure 3: Discretization of pumpkin gore configurations: (a) $G_F \in \mathbb{R}^2$ - flat unstrained gore panel with load tendon detached; $0 \leq v \leq L_c$ where L_c is the length of the centerline; L_t is the tendon length. (b) $\mathcal{G}_F \in \mathbb{R}^3$ - theoretical pumpkin gore as determined by shape finding process (centerlines of G_F and $\mathcal{G}_F$ are identical in length); (c) $\mathcal{S}_F \in \mathbb{R}^3$ - deformed pumpkin gore.

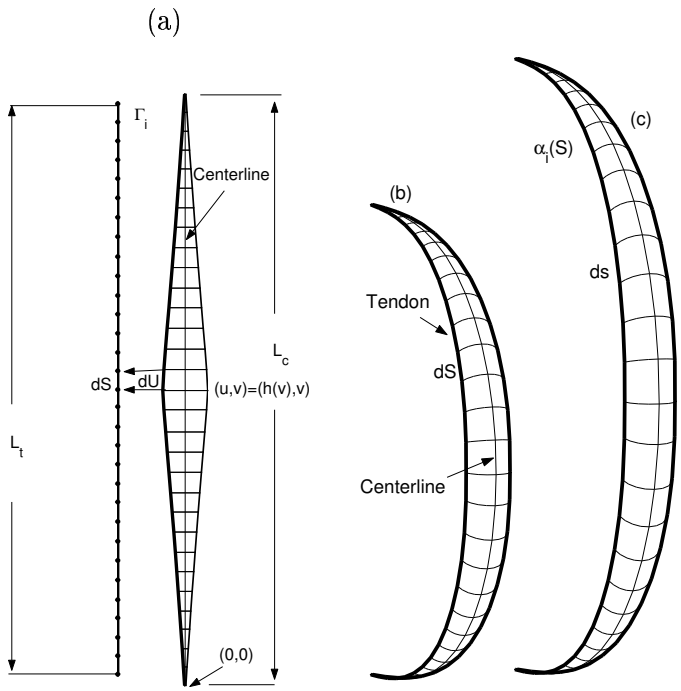

Figure 4: Euler-elastica lay-flat (dashed edges, $r_B = 0.9$) versus Endeavour lay-flat (solid, $v_B = 75$ deg). Endeavour-like pattern has more material in the mid-latitudes. In order to highlight differences, the figure is not true to scale.

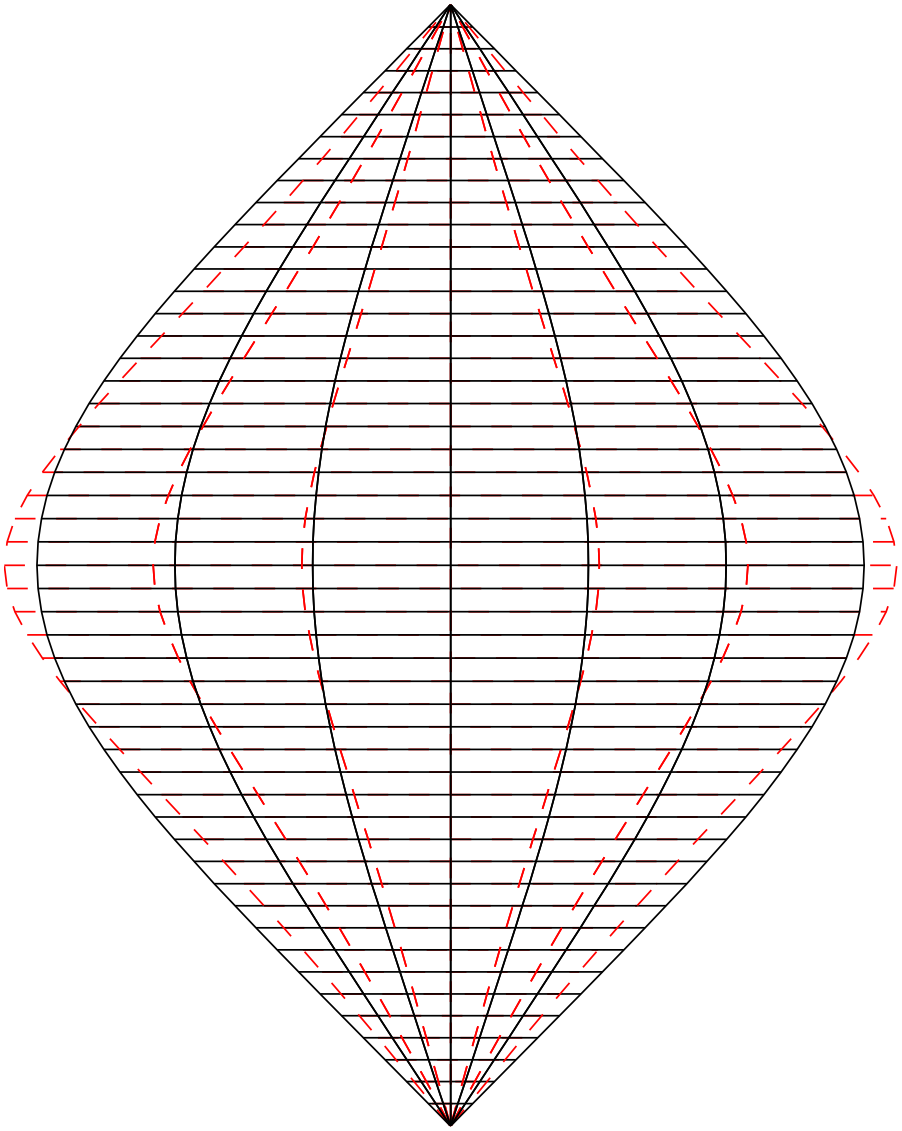

Figure 5: Stability plots for Euler-elastica constant bulge angle balloons: (a) Case 1: Nominal gore-width; (b) Case 2: Gore half-width increased by 1 cm. Calledine stability curves $n < 34/v_B^{5/2}$ and $n < 47/v_B^{5/2}$ are shown. With a half-gore-width perturbation of 1 cm, the 60 gore alternate Endeavour design is still on the border of instability. BBS is stability based on Definition 4.1.

(a) Case 1

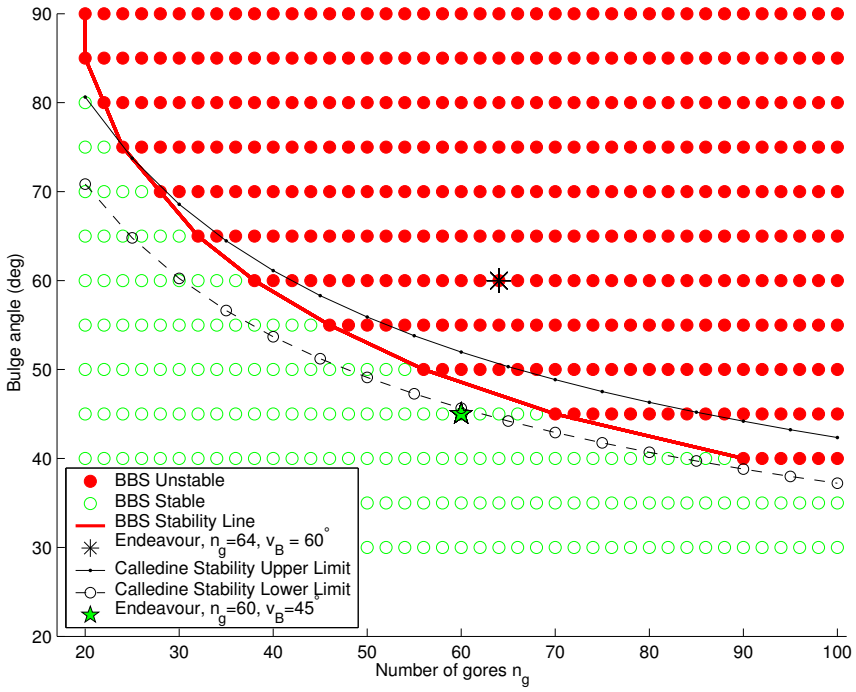

(b) Case 2

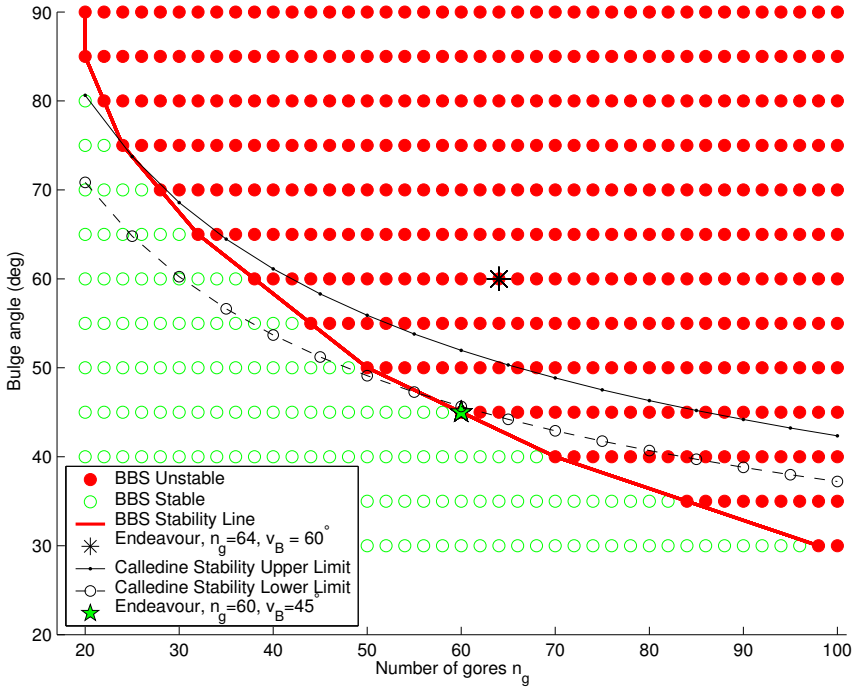

Figure 6: Stability plots for Euler-elastica constant bulge radius balloons: (a) Nominal gore-width, (n_g, r_B)-family, all feasible designs are stable; (b) Nominal gore-width, (n_g, Δ)-family, all feasible designs are stable; (c) Gore width increased by 1 cm, (n_g, r_B)-family; (d) Gore width increased by 1 cm, (n_g, Δ)-family.

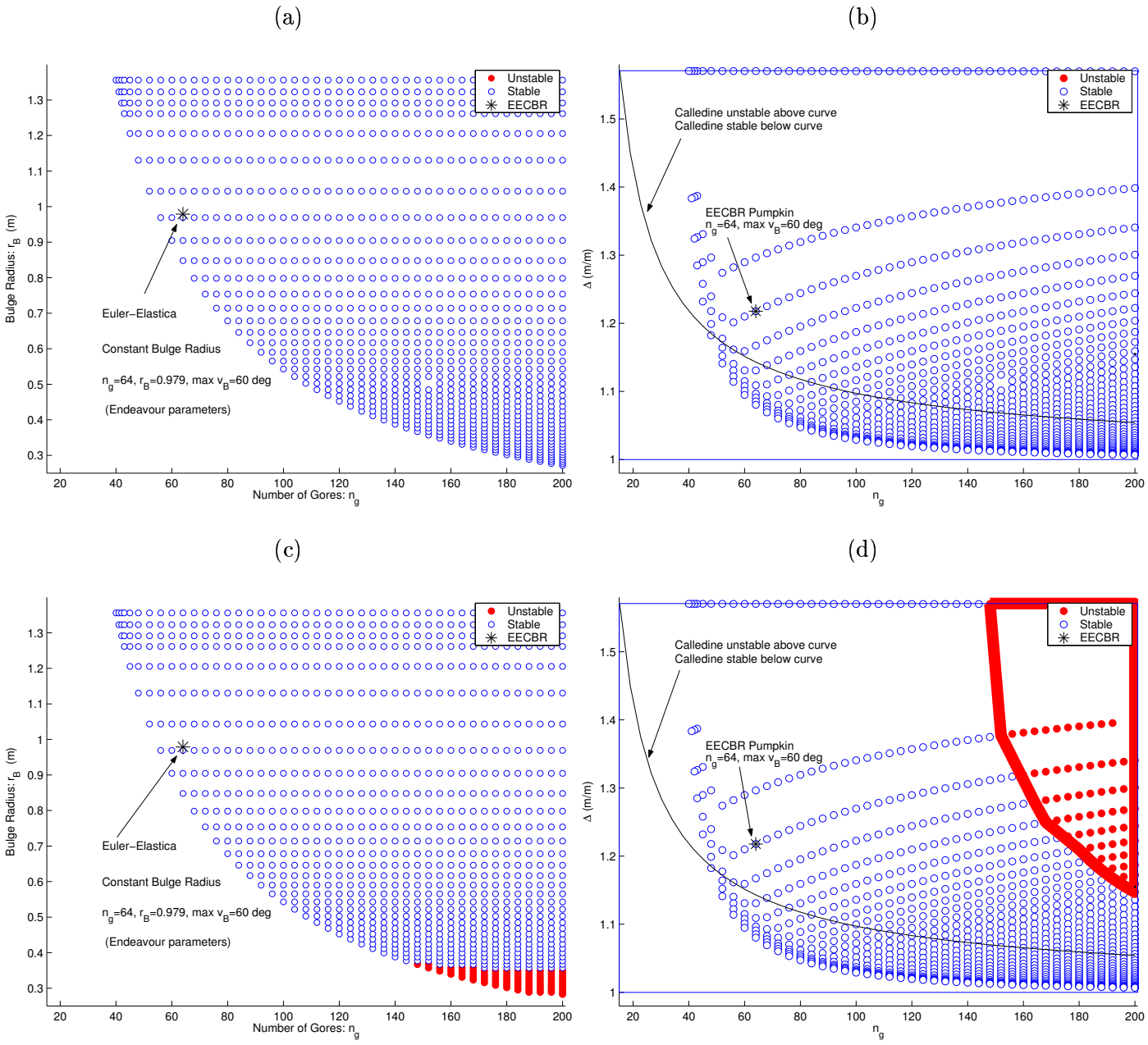

Figure 7: Fundamental half-section of an equilibrium configuration with four-fold symmetry (8 gores, one eighth of a complete balloon). Complete balloon shown in Figure 8.

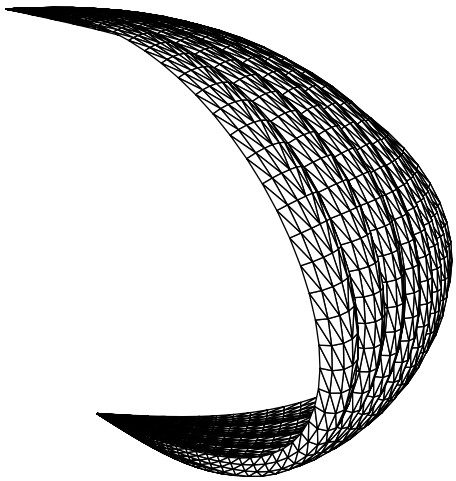

Figure 8: Equilibrium configuration with four-fold symmetry.

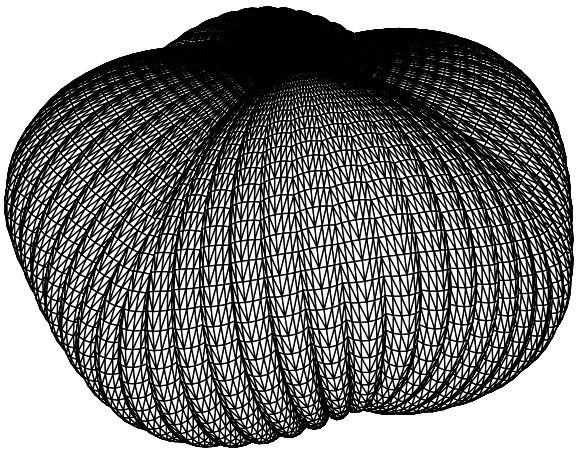

Figure 9: Equilibrium configuration with three-fold symmetry.